Covalent Attachment of Horseradish Peroxidase to Single-Walled Carbon Nanotubes for Hydrogen Peroxide Detection

*Francis Ledesma, Shoichi Nishitani, Francis J. Cunningham, Joshua D. Hubbard, Dabin Yim, Alison Lui, Linda Chio, Aishwarya Murali, and Markita P. Landry**

Single-walled carbon nanotubes (SWCNTs) are desirable nanoparticles for sensing biological analytes due to their photostability and intrinsic near-infrared fluorescence. Previous strategies for generating SWCNT nanosensors have leveraged nonspecific adsorption of sensing modalities to the hydrophobic SWCNT surface that often require engineering new molecular recognition elements. An attractive alternate strategy is to leverage pre-existing molecular recognition of proteins for analyte specificity, yet attaching proteins to SWCNT for nanosensor generation remains challenging. Toward this end, a generalizable platform is introduced to generate protein-SWCNT-based optical sensors and use this strategy to synthesize a hydrogen peroxide (H_2O_2) nanosensor by covalently attaching horseradish peroxidase (HRP) to the SWCNT surface. A concentration-dependent response is demonstrated to H_2O_2, confirming the nanosensor can image H_2O_2 in real-time, and assess the nanosensor's selectivity for H_2O_2 against a panel of biologically relevant analytes. Taken together, these results demonstrate successful covalent attachment of enzymes to SWCNTs while preserving both intrinsic SWCNT fluorescence and enzyme function. It is anticipated this platform can be adapted to covalently attach other proteins of interest including other enzymes for sensing or antibodies for targeted imaging and cargo delivery.

F. Ledesma, S. Nishitani, F. J. Cunningham, J. D. Hubbard, D. Yim, A. Lui, L. Chio, A. Murali, M. P. Landry
Department of Chemical and Biomolecular Engineering
University of California
Berkeley, CA 94720, USA
E-mail: landry@berkeley.edu
M. P. Landry
Innovative Genomics Institute (IGI)
Berkeley, CA 94720, USA
M. P. Landry
California Institute for Quantitative Biosciences (QB3)
University of California
Berkeley, CA 94720, USA
M. P. Landry
Chan-Zuckerberg Biohub
San Francisco, CA 94158, USA

1. Introduction

Single-walled carbon nanotubes (SWCNTs) possess unique optical and physical properties that make them attractive materials for biomedical applications.[1] In particular, their intrinsic photoluminescence in the near-infrared (nIR) region and lack of photobleaching are ideal traits for in vivo and ex vivo sensing and imaging in biological systems.[2,3] Another advantage of SWCNTs as nanosensors is the diversity of functionalization that add synergistic functions to the SWCNT conjugates. For instance, the functionalization of SWCNTs with biomolecules, such as single-stranded DNA (ssDNA), creates a corona phase at the proximity of SWCNT surfaces which can interact specifically with analytes of interest, resulting in modulation of the SWCNT optical signal.[4] Owing to their sequence modularity, various ssDNA sequences have been identified to play this corona phase molecular recognition (CoPhMoRe) role through screening for selective recognition of target molecules.[5] Furthermore, ssDNA can be evolved to have a selective interaction with an analyte through systematic evolution of ssDNA ligands by exponential enrichment.[6] While these ssDNA-SWCNT conjugates have shown promising analyte-specific fluorescence signal modulation, the platform fails to guarantee nanosensor generation for a specific analyte of interest as the molecular recognition element of these nanosensors is not rationally designed.

Researchers have pursued the development of semi-rationally designed polymer-SWCNT conjugates to better develop nanosensor generation for a particular analyte. For example, Bisker et al. used a small phospholipid library screen to identify the phospholipid-PEG polymer DPPE-PEG(5000) to selectively recognize fibrinogen proteins with an 80% decrease in SWCNT fluorescence intensity upon addition of fibrinogen protein.[7] Similarly, Bisker and colleagues identified another PEGylated lipid, C_{16}-PEG(2000)-Ceramide, to serve as a recognition element for SWCNT-based insulin nanosensors with a turn-off response of $\approx 60\%$.[8] Though these approaches successfully demonstrate CoPhMoRe sensing of their target analytes, they still require

**ADVANCED
SCIENCE NEWS**

www.advancedsciencenews.com

**ADVANCED
FUNCTIONAL
MATERIALS**

www.afm-journal.de

labor-intensive screens of similar polymer coating libraries to identify the optimal candidate for use as a molecular recognition element. Another approach for polymer-SWCNT nanosensors involves the use of synthetic peptide mimics named peptoids, which feature N-substituted side chains that confer both resistance to protease degradation and sequence tunability to rationally design molecular recognition. Chio et al. demonstrated the utility of these polymers by designing a small peptoid library and identifying a peptoid with both hydrophobic anchor sequences to bind to the SWCNT surface and loops of side chains designed to selectively bind the target protein Wheat Germ Agglutinin.[9] While this system successfully showed the ability to rationally design polymer-SWCNT nanosensors, the need for extensive library screens to identify successful molecular recognition elements remains a limitation to using pre-existing molecular recognition elements for nanosensor development. Overall, there are several advantages of polymer-SWCNTs for nanosensor development, including the development of nanosensors for which there exist no natural molecular recognition elements and the tunability of their selectivity and sensitivity profiles often achievable with more extensive screening.

Direct attachment of known molecular recognition elements such as proteins to SWCNTs present an orthogonal method for nanosensor generation that can circumvent some of the drawbacks of polymer-SWCNT screening, including time and cost of screening for nanosensor sensitivity, limited nanosensor selectivity, and less straightforward mechanistic function of the resulting nanosensor. Given their natural affinity for binding a target analyte, proteins are often the most readily available molecular recognition elements with which to develop nanosensors through protein-SWCNT conjugation.[10] While protein-SWCNT nanosensors can be rationally designed to detect or image a variety of biomarkers, the major drawback is that protein attachment to SWCNTs often compromises protein stability or SWCNT fluorescence.[11–13]

Traditionally, protein-SWCNT conjugates have been prepared by non-covalent approaches.[14] These methods typically rely on physical adsorption of the hydrophobic domains of proteins to SWCNT surfaces. For example, ultrasonication of SWCNT and protein[15] or dialysis-based ligand exchange[16] facilitates the non-specific adsorption of proteins to SWCNT surfaces. These non-covalent approaches, however, are dependent on the nature of the proteins which leads to varying levels of adsorption; thus, they are not generalizable.[17] Moreover, non-covalent attachment is often accompanied by conformational changes in the proteins, leading to the loss of their biological functions.[14] For example, Palwai et al. reported a complete loss of enzymatic activity of horseradish peroxidase (HRP) five days after immobilization on SWCNT.[18] A random alignment of the proteins on SWCNT may also reduce the efficiency of their biological activities, even if conformational stability is maintained. Therefore, non-covalent approaches are not a generalizable approach to developing protein-SWCNT nanosensors.

In this regard, covalent functionalization of proteins to SWCNT promises better stability and controlled alignment of the conjugated proteins.[19,20] However, covalent functionalization of SWCNT for sensing and imaging applications has been challenging because covalent bonds can introduce unintentional sp³ defects into the sp² SWCNT lattices. While certain engineered

SWCNT defects are used to shift SWCNT fluorescence for defect-based sensing, when introduced unintentionally, these defects often attenuate or fully eliminate the optical transitions in SWCNTs that drive SWCNT photoluminescence.[21,22] On the other hand, recent reports have shown successful covalent conjugation of proteins and peptides to SWCNTs while preserving their optical properties. For example, it has been shown that minimal introduction of quantum defects can preserve or even enhance the photoluminescence of SWCNTs.[23,24] Following these findings, Mann et al. developed a protocol to covalently conjugate proteins to SWCNT by controlling the density of quantum defects.[25,26] An alternative approach is to covalently functionalize SWCNTs without introducing sp³ defects using azide-based conjugation.[27,28] Since the azide-based covalent bonds do not introduce an sp³ defect by re-aromatizing the sp² lattice, this approach has a significantly higher degree of freedom in the density of functionalization compared to the approaches that use quantum defects. Recently, we have applied this chemistry to develop a versatile protocol to covalently functionalize SWCNTs and showed the potential of this chemistry to maintain analyte-specific responses of previously-reported nanosensors.[29]

In this study, we expand azide-based conjugation to develop new protein-based nanosensors by employing HRP as a model protein for the detection of hydrogen peroxide (H_2O_2). H_2O_2 is a critical component of reactive oxygen species (ROS) that play a pivotal role in many industrial and biological processes including ecosystem regulation in surface water, sterilization in food and beverage products, and cellular oxidative stress and signaling.[30,31] Consequently, developing fluorescent nanosensors for H_2O_2 that can be used for hydrogen peroxide detection or imaging is valuable, particularly non-photobleaching probes. To this end, we first developed and optimized a protocol to generate covalent HRP-SWCNT conjugates using azide-based triazine chemistry. We demonstrate that covalent conjugation does not compromise the photoluminescence properties of SWCNTs or the enzymatic activity of HRP, resulting in a robust turn-on fluorescence modulation upon nanosensor exposure to H_2O_2. Finally, we immobilized the nanosensors to show their potential applicability in bioimaging applications. Our results confirm that azide-based triazine chemistry can be used to develop new nanosensors via direct protein-SWCNT conjugation in a potentially generalizable platform, without compromising SWCNT fluorescence.

2. Results and Discussion

2.1. Nanosensor Platform Generation and Characterization

To synthesize our nanosensors, we first covalently modified unfunctionalized (pristine) SWCNTs with the azide-based triazine approach as previously reported (**Figure 1a**).[27,29] Briefly, we reacted pristine SWCNTs with cyanuric chloride and sodium azide to produce high density triazine-labelled SWCNTs (Trz-H-SWCNTs) with minimal quantum defects, maintaining intrinsic SWCNT optical properties like nIR fluorescence emission. Trz-H-SWCNTs were further functionalized with the amino acid cysteine in the presence of triethylamine. Nucleophilic substitution of the solvent-exposed chlorines on the triazine handles with the primary amine of cysteine produced thiol-functionalized
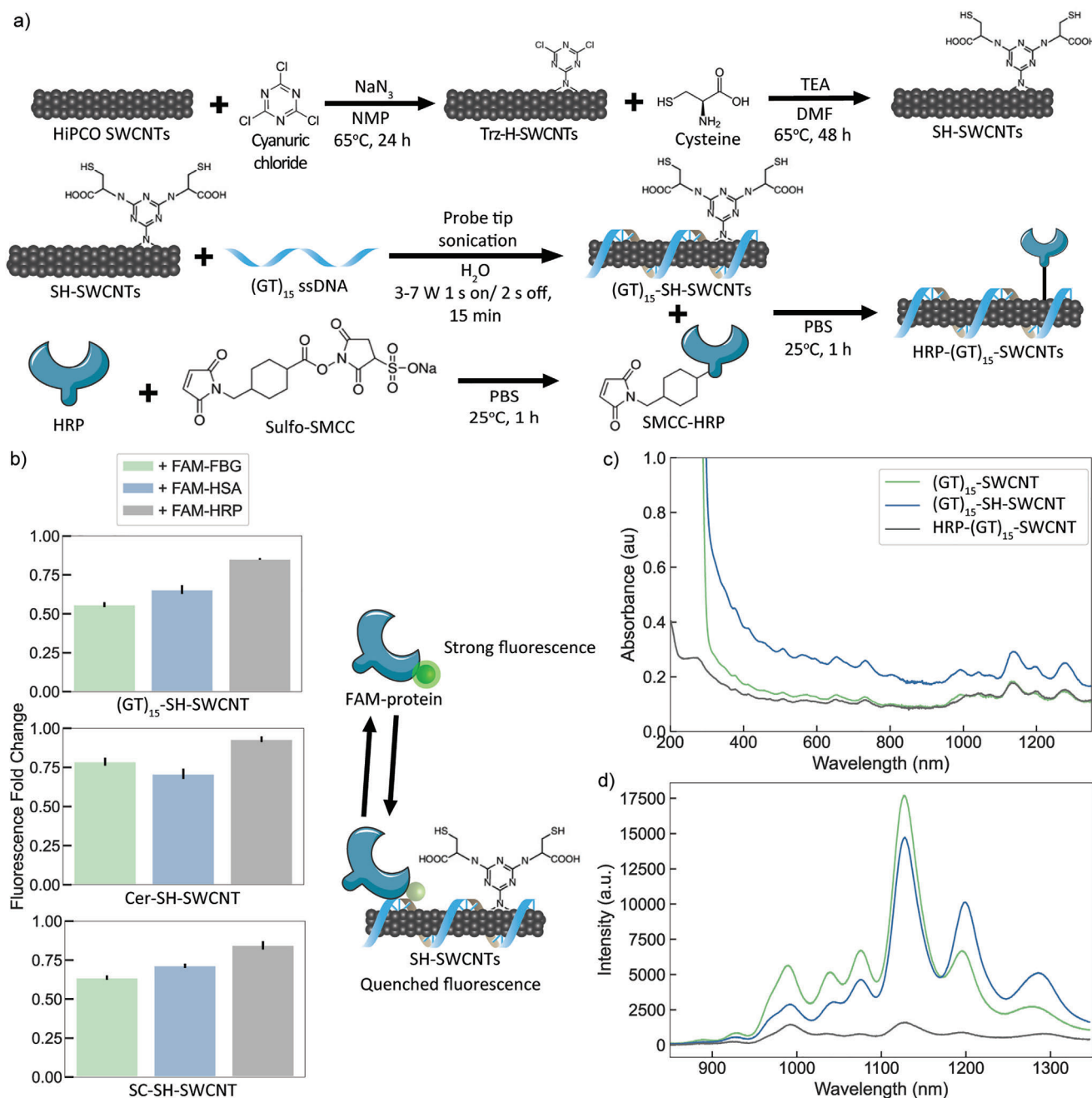
ADVANCED
SCIENCE NEWS
www.advancedsciencenews.com

ADVANCED
FUNCTIONAL
MATERIALS
www.afm-journal.de

Figure 1. Synthesis and characterization of HRP-$(GT)_{15}$-SWCNT nanosensors. a) Synthesis scheme for nanosensor performed according to previously established protocols. The SMCC:HRP ratio was optimized for single maleimide addition (Figure S1, Supporting Information) and reaction time and temperature were selected according to manufacturer protocol. Excess reactants were filtered away after each step and the final product was diluted back to the starting reaction volume. b) Corona exchange assay for HRP and control proteins shows minimal HRP adsorption to different dispersant-SH-SWCNT samples. Fold change was calculated as the endpoint FAM fluorescence value 60 min after SWCNT addition to FAM-proteins divided by the initial FAM fluorescence for each protein sample. Error bars represent the standard deviation of experimental replicates ($n = 3$). c) Absorbance spectra of $(GT)_{15}$-coated SWCNTs along the nanosensor synthesis route show maintained characteristic peaks. d) nIR fluorescence baselines for the samples in (c) show preservation of SWCNT intrinsic fluorescence throughout synthesis.

SWCNTs (SH-SWCNTs). These SWCNTs maintained their optical properties as shown by the preservation of characteristic absorbance (Figure 1c) and fluorescence (Figure 1d) peaks. Notably, the choice of cysteine for functionalization was made in part due to Sulfo-SMCC being chosen as the cross-linker for this protein-

SWCNT conjugation. This cross-linker is optimal for this conjugation scheme as it features two orthogonal functional groups: an N-hydroxysuccinimide-ester group (NHS-ester) that first reacts with solvent-exposed primary amines on HRP and a maleimide group that subsequently forms a stable covalent bond with free

thiol groups on the SWCNT. This stepwise order of cross-linking afforded by Sulfo-SMCC helps minimize unwanted side reactions and imparts the flexibility of extending this platform to conjugate other proteins with exposed primary amines with the same SH-SWCNT sample.

To solubilize SH-SWCNTs for conjugation with HRP, we assessed 3 potential amphiphilic SWCNT dispersants: $(GT)_{15}$ ssDNA, the amphiphilic lipid C_{16}-PEG(2000)-Ceramide (Cer), and the surfactant sodium cholate (SC). We induced noncovalent adsorption of each coating with SWCNTs through $\pi-\pi$ aromatic stabilization and hydrophobic attraction, respectively. Each dispersant was added to SH-SWCNTs and subjected to probe-tip sonication on ice according to previously established protocols.[29,32] The resulting products ($(GT)_{15}$-SH-SWCNT, Cer-SH-SWCNT, and SC-SH-SWCNT) showed high yield (100–300 mg L^{-1}) and solubility in water after centrifugation to remove aggregates and excess dispersant (Figure S2a, Supporting Information).

The solubilized SWCNT products were subsequently assessed for the degree of nonspecific HRP adsorption to their surface with a corona exchange dynamics assay.[17] Briefly, this assay leverages the fluorescence quenching effect of fluorophores proximal to SWCNT to measure the degree of nonspecific protein adsorption to SWCNT surfaces. Compared to fluorescein (FAM)-functionalized control proteins fibrinogen (FBG-FAM) and human serum albumin (HSA-FAM), HRP-FAM showed lower FAM fluorescence quenching when incubated with SWCNTs, indicated by a higher endpoint fluorescence fold change value (Figure 1b). Since the degree of FAM quenching is proportional to the amount of nonspecific protein adsorption to the SWCNT surface, our results suggest that HRP shows minimal nonspecific adsorption to all three dispersed SWCNTs. This result highlights the utility of HRP as a model protein as its low level of adsorption helps ensure subsequent SWCNT sensor responses can be attributed to covalently attached HRP only, rather than a mixed population of covalently-attached and nonspecifically-adsorbed HRP. Though all three dispersants were good candidates in minimizing nonspecific HRP adsorption, we proceeded with H_2O_2 nanosensor development with $(GT)_{15}$-SH-SWCNTs as they showed greater colloidal stability than SC-SH-SWCNTs through the rest of the sensor's synthesis (Figure S3a, Supporting Information) and greater response to H_2O_2 than Cer-SH-SWCNTs (Figure S4a, Supporting Information).

The covalent cross-linker Sulfo-SMCC was chosen to functionalize HRP with solvent-accessible maleimide groups for subsequent conjugation to $(GT)_{15}$-SH-SWCNTs (Figure 1a). We reacted the NHS-ester group of Sulfo-SMCC with solvent-exposed primary amines on HRP to form maleimide-functionalized HRP (SMCC-HRP). There are 6 solvent-exposed primary amines in the form of lysine residues on the surface of HRP, 3 of which are the most amenable to cross-linker functionalization (K232, K241, K174).[33] The other 3 lysines are either involved in salt bridges (K65 and K149) or barely exposed to solvent (K84).[34] As such, we expected to add between 1 and 3 SMCC cross-linkers to HRP under these reaction conditions. Optimizing the SMCC:HRP ratio during the conjugation reaction via QTOF-MS shows successful addition of 1 SMCC for a 10:1 SMCC:HRP ratio and the appearance of dual functionalization at a higher ratio of 20:1 (Figure S1, Supporting Information). As all 3 potential lysines are not located within the binding pocket of HRP and subsequent activity assays

show negligible loss in enzymatic activity post-SMCC functionalization, the exact identity of which lysine is modified was left unknown, though previous literature suggests the most reactive lysine of the potential candidates is K232.[34] Thus, we concluded that the optimal ratio of SMCC:HRP is 10:1 as it leads to singular functionalization, though this ratio would need re-optimization for any new protein to be used with this strategy depending on its number and availability of solvent-exposed primary amines.

After de-salting excess unreacted cross-linker, we reacted SMCC-HRP with $(GT)_{15}$-SH-SWCNTs to covalently link HRP to SWCNTs. Following centrifugal membrane filtration to remove excess unreacted SMCC-HRP (Figure S5, Supporting Information), we characterized the final nanosensor product (HRP-$(GT)_{15}$-SWCNT). The nanosensor showed maintained characteristic optical absorbance (Figure 1c) and fluorescence (Figure 1d) properties of SWCNT throughout the synthesis process. The different peaks in Figure 1d correspond to different chiralities of SWCNT, which emit fluorescence at different intensities in response to our excitation laser at 721 nm. This monochromatic laser predominantly excites the (10,2), (9,4), (8,6), (10,5), and (8,7) chiralities more efficiently than chiralities that resonate at lower excitation wavelengths, resulting in the largest emission peaks at wavelengths greater than 1100 nm. The relative intensities of these emission peaks were slightly altered following triazine functionalization for $(GT)_{15}$-SH-SWCNT compared to pristine $(GT)_{15}$-SWCNT, where the (9,4) and (8,6) chirality SWCNTs showed increased emission intensity at 1135 and 1195 nm, respectively, relative to the other chirality peaks at shorter wavelengths. This is expected from previous literature findings that the triazine functional group modifies the SWCNT chemical potential, increasing emission intensity for these chiralities at our excitation wavelength of 721 nm.[27] To account for these different chirality effects, we opted to analyze the nanosensor response by measuring the area under the fluorescence emission curve by integrating from 850 to 1350 nm rather than measuring the intensity at any single chirality peak wavelength.

We found that attaching HRP to SWCNTs yielded a decrease in fluorescence intensity proportional to the concentration of HRP in the conjugation reaction, with minimal shifts in the SWCNT fluorescence peak wavelengths for HRP-$(GT)_{15}$-SWCNT relative to the base $(GT)_{15}$-SH-SWCNT material (Figure S6b, Supporting Information). This uniform decrease in fluorescence intensity is a desired and common mechanism to generate turn-on fluorescent nanosensors.[35] Since the observed quenching is proportional to the amount of HRP available for conjugation, we hypothesize that HRP is affecting SWCNT fluorescence emission by proximity to the surface upon conjugation, leading to greater attenuated fluorescence intensity as more HRP is conjugated. If this attenuation was due to unintended quantum defects or other sp^2 lattice damage introduced by the synthesis process, the SWCNT fluorescence intensity would not be modulated in the presence of the HRP substrate H_2O_2 but instead remain attenuated. Subsequent experiments show that the resulting nanosensors can modulate in fluorescence and exhibit different fluorescence responses to the addition of H_2O_2, with the highest magnitude of fluorescence increase achieved with the nanosensor generated with 1 mg mL^{-1} HRP in the conjugation reaction (Figure S6a, Supporting Information). Additionally, previous studies have shown that SWCNT fluorescence intensity

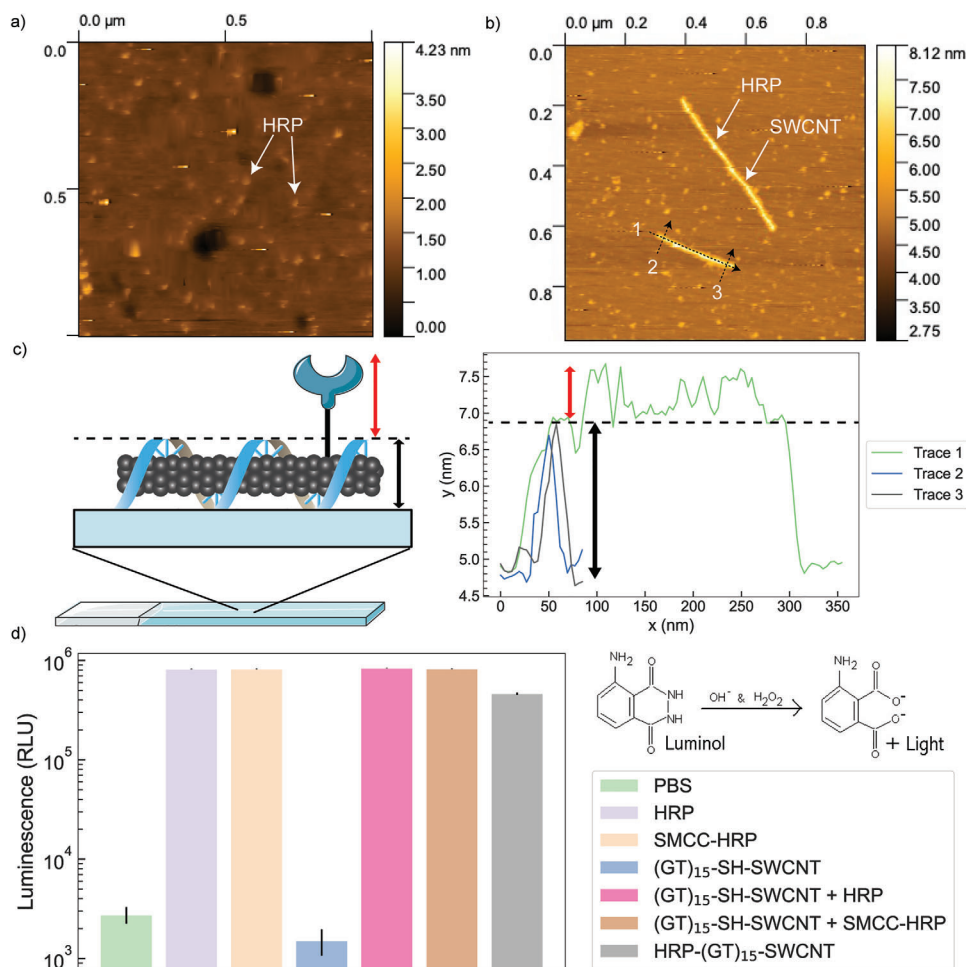**ADVANCED**
SCIENCE NEWS

www.advancedsciencenews.com

ADVANCED
FUNCTIONAL
MATERIALS

www.afm-journal.de

Figure 2. Validation of HRP presence and activity for HRP-(GT)$_{15}$-SWCNT nanosensors. a) AFM image of HRP. Height trace analysis shows a height increase of ≈0.7 nm for this protein when accounting for the surface baseline (Figure S7, Supporting Information). b) AFM image of nanosensor shows individual SWCNTs with several height spikes along axis, visually confirming both successful (GT)$_{15}$ dispersion (minimal aggregates) and HRP conjugation. c) Height trace analysis of the AFM image in (b) shows that the height spikes along the SWCNT axis (Trace 1) correspond to HRP height above SWCNT baseline (Trace 2,3). d) Luminol activity assay shows nanosensor has comparable HRP activity to control and that neither SMCC functionalization nor SWCNT presence interferes with HRP activity. Error bars represent the standard deviation between experimental replicates (*n* = 3).

decreases in the presence of H_2O_2 rather than increase, providing further evidence that the catalysis of H_2O_2 by HRP facilitates the turn-on fluorescence response.[36]

Mechanistically, we hypothesize that the SWCNT quenching upon HRP conjugation could be attributed to a proximity effect of the charged heme center of HRP or HRP itself on SWCNT fluorescence emission. SWCNT fluorescence occurs by exciton recombination, where an electron in the valence band of SWCNT is photo-excited by visible light, creating an excited electron-hole pair (exciton), and subsequently decays back to its ground state, recombining with the empty hole in the SWCNT valence band and emitting fluorescence.[37,38] As such, positively charged groups near the SWCNT surface could effectively serve as a charge trap, locally stabilizing excitons and lowering the exciton energy below the threshold needed for radiative recombination and fluorescence emission.[39] At its native state, the heme iron of HRP exists as Fe^{3+} and the proximity of this positively charged metal ion to the SWCNT surface could lower exciton recombination energy, resulting in nonradiative electron decay and fluo-

rescence quenching. Previous literature supports this possibility, demonstrating that free metal ions,[40] ferricyanide,[11] and free heme[41] added to SWCNTs strongly quench their fluorescence by this nonradiative mechanism. Similarly, HRP exhibits an isoelectric point (pI) between pH 8.7 and 9,[42] resulting in a net positive (+2) charge at neutral pH.[43] Thus, HRP itself could also serve as a charge trap and quench SWCNT fluorescence by the same nonradiative decay mechanism.

After developing and optimizing the reaction conditions for this sensor, we characterized its physical and chemical properties to confirm the successful covalent attachment of HRP to SWCNTs while maintaining enzymatic activity. To visualize HRP on the surface of SWCNTs, we captured atomic force microscopy (AFM) images of HRP (**Figure 2a**) and HRP-(GT)$_{15}$-SWCNT (Figure 2b). Height trace analysis over 10 of the clearest proteins and subtracting the height of the bare surface yielded an average height of 0.66 nm for HRP under these conditions (Figure S7, Supporting Information). Performing the same analysis along the length of the nanotube showed several peaks of

**ADVANCED
SCIENCE NEWS**

www.advancedsciencenews.com

**ADVANCED
FUNCTIONAL
MATERIALS**

www.afm-journal.de

increased height ≈0.7 nm greater than the height of the nanotube as determined by tracing perpendicular to the SWCNT length axis (Figure 2c). Combined with the corona exchange results confirming minimal nonspecific adsorption of HRP to SWCNTs, these peaks can thus be attributed to covalently attached HRP as shown schematically (Figure 2c).

To confirm that covalently attached HRP maintained enzymatic activity while on the surface of SWCNTs, we used a luminol assay according to established protocols.[44] Briefly, the oxidation of luminol by the catalysis of H_2O_2 by HRP produces luminescence proportional to protein activity when normalized for protein concentration. We thus measured luminescence values for all HRP conditions along the nanosensor synthesis route incubated with luminol and H_2O_2 (Figure 2d). Compared to the low luminescence magnitude shown by the controls of empty wells (Figure S8, Supporting Information), PBS, and $(GT)_{15}$-SH-SWCNT alone, the nanosensor showed similar catalytic activity to the other HRP-containing samples at the same protein concentration. This data also suggests that SMCC functionalization does not negatively affect HRP activity under these conditions. Similarly, the presence of SWCNT showed little negative impact on the activity of both native and SMCC-HRP when mixed. Furthermore, we measured the enzymatic activity of our nanosensor over the course of 20 days, observing no noticeable decrease in luminescence (Figure S8, Supporting Information).

We also leveraged the luminol assay to calculate the concentration of HRP in each sample by using the luminescence values of a calibration curve of known HRP concentrations to extract a linear regression model (Figure S9b, Supporting Information). Using the luminescence of the nanosensor with this model calculated an approximate HRP concentration of 0.415 µg mL^{-1} in the sample (Figure S9c, Supporting Information). Since the concentration of SWCNT in the nanosensor sample can be determined by the absorbance at 632 nm (Figure S9d, Supporting Information), we converted both values to moles by the known molecular weights of HRP (44 kDa) and SWCNT (2700 kDa) and divided the two to roughly approximate the number of HRP per SWCNT in the nanosensor at 80.5 ± 8.4 (Figure S9e, Supporting Information). Taken together, these results suggest that we have synthesized a stable covalent HRP-SWCNT sensor with preserved SWCNT and enzymatic properties that can be assessed for its ability to sense hydrogen peroxide.

2.2. Characterizing Nanosensor Response to Analyte Hydrogen Peroxide

We characterized our HRP-$(GT)_{15}$-SWCNT nanosensor's response to hydrogen peroxide by measuring the change in nIR SWCNT fluorescence over time in response to varied levels of H_2O_2 analyte, schematically represented in **Figure 3a**. The addition of 29.4 mM H_2O_2 elicited a strong and stable turn-on fluorescence response over the course of 1 h (Figure 3c). This contrasts with the minor turn-off response elicited by water (Figure 3b), isolating the analyte as the cause of the turn-on response rather than the addition of volume to the sample. The normalized integrated change in fluorescence ($\Delta F/F_0$) of the sensor peaked af-

ter 20 min post-addition of H_2O_2 and remained stable over the course of 1 h (Figure 3d).

In contrast, $(GT)_{15}$-SH-SWCNT alone exhibits a turn-off fluorescence response to H_2O_2 (Figure S10a, Supporting Information), as expected from previous literature.[36] Furthermore, HRP mixed with $(GT)_{15}$-SH-SWCNT exhibits a strong turn-off response immediately upon H_2O_2 addition followed by a gradual increase in fluorescence to the baseline intensity (Figure S10a, Supporting Information). This non-monotonic fluorescence modulation could be due to the consumption of H_2O_2 by free HRP, mitigating the analyte's quenching effect as it is depleted from the solution. To confirm this hypothesis, we probed the response of $(GT)_{15}$-SH-SWCNTs to H_2O_2 when mixed with HRP and Catalase, a peroxide-scavenging enzyme, as well as with both proteins inactivated by glutathione (GSH), an inhibitor of HRP enzymatic activity (Figure S10b, Supporting Information).[45,46] Upon addition of 588 µM H_2O_2 to the Catalase sample, an immediate strong turn-off response is observed followed by a gradual increase in fluorescence. This response is similar to that of HRP mixed with $(GT)_{15}$-SH-SWCNTs, though lesser in magnitude as Catalase is known for having low affinity for H_2O_2 with a K_M value between 10–30 mM which would lead to less peroxide consumption over the same time period compared to HRP, thus lessening the increase in fluorescence.[47] When GSH is added to both samples to inhibit the enzymatic reaction and 588 µM H_2O_2 is added, a strong turn-off response is again observed and remains stable over time as the enzymes are unable to remove the quenching H_2O_2 from solution. Altogether, this confirms that the response observed by the sample with HRP noncovalently adsorbed to $(GT)_{15}$-SH-SWCNTs is due to consumption of quenching H_2O_2 which returns the sensor to baseline fluorescence. Thus, these results suggest that the strong turn-on response of our sensor must be due to the interaction between H_2O_2 and covalently-attached HRP on the SWCNT surface rather than between H_2O_2 or catalysis reaction byproducts and the SWCNT itself.

Furthermore, we conducted a mock synthesis where the cross-linker Sulfo-SMCC was omitted from the otherwise normal synthesis route and assessed the product (Figure S11, Supporting Information). The mock SWCNT showed notably lower HRP enzymatic activity than the nanosensor and no turn-on response to H_2O_2, emphasizing the necessity of covalent HRP conjugation to SWCNT via Sulfo-SMCC cross-linker for the nanosensor's function.

We further measured the concentration-dependent nanosensor response and determined a 31 µM limit of detection (LOD) for hydrogen peroxide (Figure 3e). The data was fit to a cooperative binding model and extracted parameters include an equilibrium constant K_A of 1.905 mM and Hill coefficient n of 1.087, as expected of this noncooperative enzyme which uses its heme cofactor to bind one peroxide molecule at a time for catalysis.[48] When compared with similar peroxide sensors, our nanosensor LOD and linear range fall within the range of literature values (**Table 1**). Though our nanosensor has a higher LOD and linear range than some systems (Figure S12, Supporting Information), our system maintains the advantages of facile synthesis, form factor variability, non-photobleaching nature, and an underlying platform that
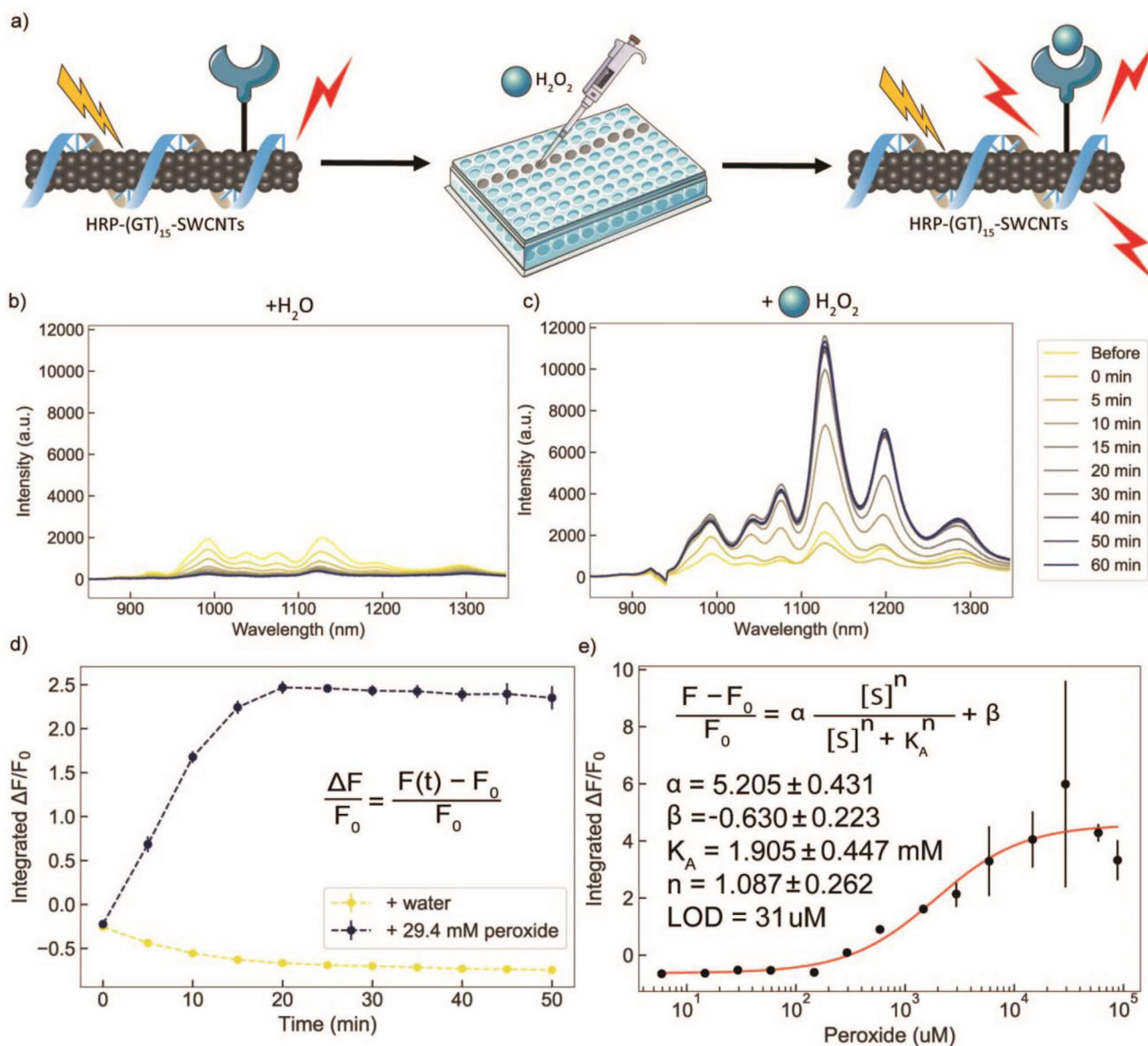
ADVANCED
SCIENCE NEWS

www.advancedsciencenews.com

ADVANCED
FUNCTIONAL
MATERIALS

www.afm-journal.de

Figure 3. HRP-(GT)$_{15}$-SWCNT nanosensor response to H$_2$O$_2$ in solution-phase screen. a) Schematic depiction of response screening platform, where addition of analyte to a 384-well plate with nanosensor induces a strong turn-on response as measured by the increase in nIR fluorescence emission. b) Nanosensor response to water shows a strong turn-off response over 60 min. c) Nanosensor response to 29.4 mM H$_2$O$_2$ shows a strong turn-on response over 60 min. d) The normalized integrated change in fluorescence ($\Delta F/F_0$) for (b) and (c). F_0 is set to the integrated fluorescence intensity of the "Before" baseline timepoints in (b) and (c) taken immediately prior to H$_2$O$_2$ addition. e) Endpoint (time = 60 min) $\Delta F/F_0$ values for varying concentrations of analyte plotted and fit to a cooperative binding model. Fit parameters are listed with 95% confidence intervals evaluated using the t-distribution. All fluorescence measurements were obtained with a laser excitation wavelength of 721 nm. Error bars represent the standard deviation between experimental replicates ($n = 3$).

is flexible enough to accommodate other proteins and analytes to generate other nanosensors or multiplexed sensors.

2.3. Investigating the Mechanism of Nanosensor Fluorescence Modulation

To further probe a potential mechanism for the nanosensor's turn-on response, we investigated the response to H$_2$O$_2$ when subjected to various conditions including high and low pH, high and low ionic strength, incubation with GSH, and incubation with Catalase. We hypothesize that the nanosensor would respond differently to H$_2$O$_2$ under these conditions by affecting HRP enzymatic activity, thus confirming the reliance on HRP enzymatic activity for the observed fluorescence turn-on response. Increasing or decreasing pH and ionic strength would increase or decrease HRP activity, respectively, the addition of GSH would inhibit enzymatic activity, and the addition of catalase would

Table 1. Comparisons of similar H_2O_2 nanosensors found in literature.

Platform	Signal Type	Linear Range [μM]	LOD [μM]	Refs.
HRP/Os Polymer	Amperometric	1–500	0.3	[49]
HRP/Au	Amperometric	40–100	40	[50]
SWCNT/GCE	Amperometric	1900–24000	1000	[51]
HRP/Luminol	Chemiluminescence	100–3000	667	[52]
Fe-N-C Nanozyme	Chemiluminescence	500–100000	0.5	[53]
Cobalt-CNT/GOx	Fluorescence	0.2–20	0.1	[54]
ssDNA-SWCNT	Fluorescence	10–1000	0.1	[36]
AgNP	Absorbance	10–10000	10	[55]
HRP-SWCNT	Fluorescence	150–600	31	This work

Abbreviations: Ag, silver; Au, gold; Fe, iron; N, nitrogen; C, carbon; GCE, glassy carbon electrode; GOx, glucose oxidase, Os, Osmium.

provide an additional H_2O_2 scavenger, reducing the amount of H_2O_2 available in solution for catalysis by HRP.

The nanosensor responds to H_2O_2 similarly in 1X PBS and 1 M NaCl, representing a higher ionic strength buffer than 1X PBS at 150 mM NaCl (Figure S13a, Supporting Information). In contrast, the nanosensor shows no response in the low ionic strength conditions of 10 mM NaCl and the zwitterionic buffer HEPES. Since previous studies have reported better HRP enzymatic activity in higher ionic strength conditions,[56,57] these results point toward the catalytic reaction as the source of the fluorescence mechanism. Furthermore, the sensor shows no response in pH 5 PBS, a normal response at pH 7, and a fast and high magnitude response at pH 9. This supports previous studies that found minimal HRP enzymatic activity at acidic pH and peak enzymatic activity from pH 8–9, as the pK_a of HRP is ≈8.6.[56–58] Together, these results suggest that the optimal conditions for nanosensor response are at high pH and ionic strength, conditions that optimize HRP enzymatic activity. Therefore, mechanistically, these results support a nanosensor mechanism whereby HRP enzymatic consumption of H_2O_2 drives an increase in SWCNT fluorescence.

To further support this mechanistic nanosensor function, when HRP is noncovalently mixed with SWCNTs in the aforementioned conditions rather than covalently attached to the SWCNT surface as in our nanosensor, the noncovalently mixed samples show no turn-on response (Figure S13b, Supporting Information). Lastly, as an orthogonal method to support this nanosensor's mechanism, our corona exchange assay (Figure 1b) and filtration of free HRP (Figure S5, Supporting Information) indicate minimal/no free HRP adsorption to SWCNTs. Taken together, these results further support that the sensing mechanism relies on the interaction between HRP and SWCNTs near the SWCNT surface enabled by covalent conjugation of HRP to the SWCNT surface.

This hypothesis is further supported by investigating the nanosensor response when incubated with GSH to inhibit HRP activity and Catalase as a separate H_2O_2 scavenger (Figure S14a, Supporting Information). Incubation with 1 mM GSH for 1 h prior to testing completely negates the nanosensor's turn-on response to H_2O_2, further suggesting that HRP enzymatic activity is necessary to modulate SWCNT fluorescence. Furthermore, ad-

dition of 0.01 mg mL^{-1} Catalase to the nanosensor shows a slower and lower magnitude turn-on response to H_2O_2 compared to the nanosensor alone, likely due to Catalase catalyzing and thus reducing the available H_2O_2 in solution for consumption by HRP on the nanosensor. The addition of free HRP to the sample at 0.01 mg mL^{-1} does not impact the nanosensor's response profile to H_2O_2, as it reaches the same peak fluorescence over the same period, highlighting the reliance of HRP proximity to the SWCNT surface for the turn-on response rather than attributing the nanosensor response to reaction byproducts or H_2O_2 consumption by free/adsorbed HRP.

With these results in hand, the remaining possible mechanisms for the turn-on response of the nanosensor can be narrowed down to: i) the redox charge state of the heme center of HRP existing at a state that enhances SWCNT fluorescence emission, ii) conformational change of HRP during the catalytic cycle causing ssDNA to shift on the SWCNT surface leading to increased fluorescence emission, or iii) HRP destruction/denaturation causing a return to SWCNT alone baseline fluorescence without the quenching effect of HRP in proximity to the SWCNT surface. To evaluate the impact of these potential mechanistic contributions to our nanosensor response, we can, respectively: i) pre-incubate the nanosensor with varying levels of H_2O_2 and test the subsequent response to varying levels of H_2O_2 to determine if HRP is induced to the inactive forms of Compound III or P-670 as described in previous literature,[59] ii) compare the nanosensor's response to H_2O_2 when wrapped with other polymers including ssDNA sequences of the same (C_{30} and T_{30}) and different (($GT)_6$) length as $(GT)_{15}$, and the amphiphilic lipid C_{16}-PEG(2000)-Ceramide, and iii) assess the nanosensor's response to a protein denaturant such as SDS which is known to denature HRP.[60]

Regarding Mechanism (i), extensive studies have been conducted to understand the catalytic cycle of HRP and the resulting oxidation state of the heme center at each intermediate stage in the cycle. Briefly, researchers have identified four possible intermediate redox states for the heme center of HRP during the catalytic cycle: Compound I, Compound II, Compound III, and P-670.[61] The typical catalytic cycle involves fast conversion to Compound I then Compound II, followed by decay to native enzyme. However under certain conditions, the enzyme can

**ADVANCED
SCIENCE NEWS**

www.advancedsciencenews.com

**ADVANCED
FUNCTIONAL
MATERIALS**

www.afm-journal.de

be converted to primarily Compound III, a catalytically inactive intermediate.[62] From this state, Compound III either slowly decays back to the native enzyme or irreversibly inactivates to its P-670 form. In particular, researchers have investigated various mechanisms for inducing HRP inactivation including heme destruction,[63] acid treatment,[64] ionizing radiation,[65] and excess H_2O_2 with no exogenous substrates,[59,66–68] as is the case with our system. We hypothesize that should Mechanism (i) be contributing to the nanosensor response, HRP on the nanosensor would be rapidly converted to Compound III or P-670 upon the addition of high H_2O_2 (29.4 mM) and this process would occur much slower at low H_2O_2 (588 μM), explaining the differences in both time and magnitude of the nanosensor's response profile in both cases. Additionally, subsequent additions of H_2O_2 to samples that have already been treated with high and low levels of H_2O_2 would induce either no response or an attenuated response, respectively, if the enzymes were indeed inactivated.

The nanosensor indeed shows the described response profile, exhibiting a rapid and high magnitude increase in fluorescence in response to 29.4 mM H_2O_2, reaching its peak increase ≈15 min post-addition and ≈450% fluorescence increase over baseline (Figure S14b, Supporting Information). Interestingly, when pre-treated with 29.4 mM H_2O_2, the nanosensor exhibits no turn-on response to both 29.4 mM and 588 μM H_2O_2, suggesting that this high amount of H_2O_2 inhibits subsequent HRP activity, supported by literature findings that excess H_2O_2 induces HRP to the Compound III and P-670 inactive states at $[H_2O_2]$ >1 mM.[59] By contrast, the nanosensor reaches a peak fluorescence increase of ≈100% after 60 min in response to 588 μM H_2O_2. When the nanosensor is pre-treated with 588 μM H_2O_2 for 1 h before screening, the nanosensor exhibits a similar response profile to 29.4 mM H_2O_2, though slower and lower in magnitude than the response without this pre-treatment, reaching a peak of ≈375% increase after 30 min. This result suggests that 588 μM H_2O_2 is not enough to fully inhibit HRP activity by converting the redox state to Compound III or P-670 since it still responds to 29.4 mM H_2O_2. On the other hand, the response to 588 μM H_2O_2 after pre-treatment with the same amount of H_2O_2 shows a decreased, but faster turn-on response of ≈50% at 0 min and remains stable for 60 min. If this response was due to cycling of the heme redox state back to native enzyme rather than settling at one state, this response would be expected to decrease back to baseline fluorescence as H_2O_2 is depleted. However, the stability of both this response and that of 29.4 mM H_2O_2 alone potentially indicates a reliance on the generation of Compound III or P-670 forms of HRP for fluorescence modulation. The magnitude of the response could thus be proportional to the fraction of HRP on SWCNT converted to these redox states and the kinetics of the response would depend on the concentration of H_2O_2 as we observe in Figure S14b (Supporting Information).

To determine if Compound III or P-670 dominates the HRP heme redox state when our nanosensor exhibits a turn-on response, we investigated the nanosensor response to H_2O_2 in the presence of salicylic acid (SA) (Figure S14c, Supporting Information). SA is known to induce P-670 formation at high H_2O_2,[69,70] so if P-670 formation is the source of fluorescence modulation in the nanosensor, the previously observed nanosensor response profile would be observed for pre-treatment with 29.4 mM H_2O_2 for 1 h before screening to induce Compound III formation

followed by addition of 1 mM SA. However, nanosensor pre-treatment with 29.4 mM and 588 μM H_2O_2 showed no response to SA, while pre-treatment with SA only induced a response for 29.4 mM H_2O_2. Additionally, addition of SA alone showed no turn-on response. Together, these results suggest that HRP on the nanosensor is primarily induced to Compound III in the presence of high H_2O_2 rather than irreversibly inactivated to P-670. Several studies also suggest the decay of Compound III to P-670 without SA present occurs on the order of hours, further supporting Compound III as the primary state of HRP in the nanosensor.[59,70]

We hypothesize that the proximity of the HRP heme center to the SWCNT may be close enough to enhance fluorescence emission, though investigating the specific physical mechanism of how this charged radical group influences SWCNT fluorescence is beyond the scope of this manuscript. The structure of Compound III is typically represented as a superoxide anion bound to the Ferric heme center, so this negatively charged radical group could potentially negate the charge-trapping effect of the heme iron on SWCNT excitonic recombination, increasing SWCNT fluorescence. Additionally, there is the possibility that superoxide can be released from the heme center and interact with SWCNTs, causing fluorescence modulation. However, our previous data showing that free HRP mixed with $(GT)_{15}$-SH-SWCNTs do not exhibit the same strong turn-on response to H_2O_2 as the nanosensor eliminates the possibility that superoxide anion released from Compound III induces fluorescence modulation (Figure S10, Supporting Information). Furthermore, direct addition of superoxide to $(GT)_{15}$-SH-SWCNTs alone does not induce fluorescence modulation (Figure S15b, Supporting Information), pointing the nanosensor's mechanism toward Compound III on the SWCNT surface enhancing SWCNT fluorescence emission. Previous literature suggests that redox active compounds like ascorbic acid induce a turn-on fluorescence response for ssDNA-SWCNTs, supporting the proposed mechanism.[12]

If Mechanism (ii) is contributing to the response of the nanosensor, the response to H_2O_2 would vary greatly depending on the identity of the amphiphilic polymer used to impart colloidal stability to the SWCNTs. To investigate this, we prepared covalent HRP-SWCNTs with $(GT)_{15}$, C_{30}, T_{30}, Ceramide, and $(GT)_6$ as dispersants and assessed their responses to 588 μM H_2O_2 (Figure S4a, Supporting Information. Compared to the nanosensor, HRP-C_{30}-SWCNTs and HRP-$(GT)_6$-SWCNTs exhibited the closest response profile, though HRP-C_{30}-SWCNTs reached its peak fluorescence increase at ≈75% after 5 min, while the nanosensor and HRP-$(GT)_6$-SWCNTs reached peaks of 90% and 60% after 60 and 30 min, respectively. By contrast, HRP-Cer-SWCNTs showed no fluorescence modulation in response to H_2O_2, potentially validating Mechanism (ii) as at least a partial contributor to the sensing mechanism. Interestingly, HRP-T_{30}-SWCNTs showed an immediate but small turn-on response to H_2O_2, increasing ≈18% immediately and remaining stable over 60 min. This discrepancy in response despite being a DNA sequence of similar length as $(GT)_{15}$ could be attributed to low colloidal stability of the final product as seen by the disappearance of characteristic SWCNT absorbance peaks in the UV–Vis–IR absorbance spectra of HRP-T_{30}-SWCNTs (Figure S3b, Supporting Information). However, if ssDNA is indeed perturbed by the catalysis of H_2O_2 by HRP and thus modulating SWCNT

ADVANCED
SCIENCE NEWS

www.advancedsciencenews.com

ADVANCED
FUNCTIONAL
MATERIALS

www.afm-journal.de

fluorescence, the SWCNT local dielectric environment would be altered and we would expect to see an accompanying solvatochromic shift in peak intensity wavelengths of each sample that exhibits a turn-on response. We assessed this possibility by plotting the shift in peak wavelength for the (9,4) chirality SWCNT (Figure S4c, Supporting Information), which typically appears as the highest fluorescence intensity peak ≈1135 nm due to our excitation laser wavelength of 721 nm as seen in the strongly quenched baseline sensor fluorescence spectra (Figure S4b, Supporting Information). Comparing the solvatochromic shifts of nanosensor constructs that exhibited a turn-on response to H_2O_2 after 60 min, no clear trend or dependence is seen. HRP-$(GT)_{15}$-SWCNTs show a red-shifted response, HRP-C_{30}-SWCNTs exhibits almost no solvatochromic shift, and HRP-$(GT)_6$-SWCNTs show a slight blue-shift response. By contrast, both HRP-T_{30}-SWCNTs and HRP-Cer-SWCNTs show slight blue-shifts in the (9,4) chirality wavelength despite showing minimal or no response to H_2O_2, respectively. Taken together, these results help eliminate Mechanism (ii) as a potential contributor to the observed turn-on response as the identity of the ssDNA dispersant does not significantly affect the turn-on response capability, mostly serving to impart colloidal stability on the final nanosensor constructs.

Notably, the lack of H_2O_2 response by HRP-Cer-SWCNTs without the possibility of Mechanism (ii) warrants further investigation. This could potentially be attributed to the structure of Ceramide when wrapped around SWCNTs, where the large hydrophobic lipid tails coating the nanotube surface and bulky solvent-exposed polyethylene glycol chains could sterically inhibit either analyte access to HRP or HRP physical movement needed for analyte consumption. However, despite exhibiting no turn-on fluorescence response, HRP-Cer-SWCNTs still show HRP enzymatic activity via the luminol activity assay (Figure S9a, Supporting Information). As discussed earlier, we are confident that few noncovalently adsorbed or free in solution HRP remains on SWCNTs post-synthesis, suggesting that Ceramide minimally interferes with HRP's catalytic function. In the frame of Mechanism (i), a possible explanation remains that HRP in Compound III form upon H_2O_2 addition facilitates either redox charge transfer to or otherwise influences nearby DNA bases, which has been shown in previous literature identifying particularly the guanine nucleotide as an oxidation sink, leading to fluorescence modulation.[12,71] Ceramide is presumably less redox active in this sense, potentially explaining the lack of fluorescence modulation in response to H_2O_2 despite demonstrated HRP enzymatic activity.

Finally, if Mechanism (iii) was significantly contributing to the observed nanosensor fluorescence response, we expect that the addition of a protein denaturant such as SDS would exhibit a response profile like that of H_2O_2, identifying the destruction of HRP quenching SWCNT fluorescence as the mechanistic source. Compared to the nanosensor's fast response to 29 mM H_2O_2, the addition of 35 mM SDS to the nanosensor exhibited a linear increase in fluorescence over 60 min toward a similar magnitude endpoint (Figure S16a, Supporting Information). This response was mirrored by HRP-C_{30}-SWCNT showing a similar linearity in fluorescence increase and HRP-$(GT)_6$-SWCNT exhibiting a lower magnitude but faster turn-on response, reaching peak fluorescence after 30 min. Notably, these three HRP-SWCNT con-

structs were also the only ones responsive to H_2O_2, while HRP-T_{30}-SWCNTs and HRP-Cer-SWCNTs again showed no turn-on response. Assessing the solvatochromic shift of the nanosensors in response to 35 mM SDS reveals a consistent blue-shift for all constructs except HRP-Cer-SWCNTs (Figure S16b, Supporting Information). Interestingly, the solvatochromic shift of HRP-$(GT)_{15}$-SWCNT nanosensors differs depending on the amount of H_2O_2 added, lending more support to Mechanism (i) where varying levels of H_2O_2 added induce different redox states at the heme center of HRP, affecting the local SWCNT dielectric environment and in turn increasing fluorescence. It is important to note that again, HRP-T_{30}-SWCNTs show no response to SDS in fluorescence intensity but do exhibit a strong blue solvatochromic shift, clouding the role of SDS in modulating SWCNT fluorescence and local environment. The addition of SDS to $(GT)_{15}$-SH-SWCNTs alone and when mixed non-covalently with HRP both show a strong turn-off response (Figure S16c, Supporting Information) and slight blue-shifting (Figure S16d, Supporting Information) in accordance with previous literature.[39] These results suggest that the observed response of the nanosensor to SDS cannot be attributed to SDS interacting with the SWCNT itself. Previous studies have investigated the binding and kinetics of HRP denaturation by SDS and found that at an SDS concentration of 0.60 mM, 21 moles of SDS bind to one mole of HRP.[60,72] It is thus conceivable that the observed nanosensor response to SDS can be attributed to the slow and constant binding of SDS to HRP on SWCNTs, unfolding HRP by denaturation and thereby inhibiting its ability to quench SWCNT fluorescence. However, the apparent kinetic profile of the SDS response being linear suggests that this mechanism holds true specifically for exceedingly large amounts of surfactant interacting with proteins on SWCNT rather than the general mechanism for this specific enzyme-SWCNT nanosensor.

Based on our data, we hypothesize that the leading mechanism for nanosensor function is Mechanism (i) whereby H_2O_2 modulates native HRP into different redox states that influence SWCNT fluorescence emission, namely Compound II and the Compound III inactive intermediate as has been demonstrated when H_2O_2 is the only substrate present in the reaction.[59,66,67] At high concentrations of H_2O_2, this reaction is fast and the redox active heme center of Compound III would facilitate a very strong turn-on fluorescence response accompanied by a blue-shifted fluorescence spectra by ≈5 nm. At low concentrations of H_2O_2, below the threshold required to induce Compound III formation, HRP primarily avoids Compound III formation and undergoes its regular catalytic cycle to consume added H_2O_2, cycling from native HRP to Compound I to mostly Compound II at any given time as found in previous studies.[59] With Compound II being the oxidized form of native HRP, it is possible that this redox state also enhances SWCNT fluorescence to a lesser degree than Compound III, explaining the lesser magnitude response and simultaneous red-shift in the fluorescence spectra. Since Compound II can be reduced to Compound III upon subsequent H_2O_2 addition while Compound III cannot consume H_2O_2 as it is catalytically inactive, this mechanism is compatible with our findings that the nanosensor can still increase in fluorescence after incubation with a low amount of H_2O_2 yet fails to do so after incubation with a high amount of H_2O_2.
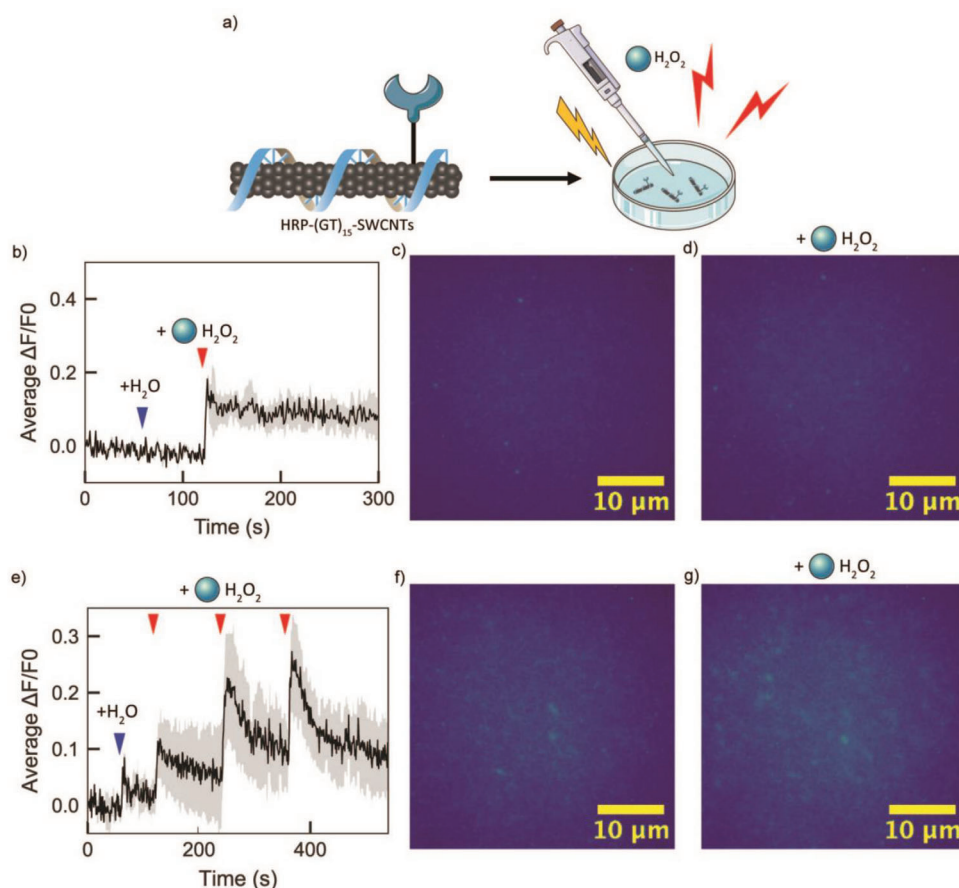
**ADVANCED
SCIENCE NEWS**

www.advancedsciencenews.com

**ADVANCED
FUNCTIONAL
MATERIALS**

www.afm-journal.de

Figure 4. Immobilized nanosensor response to H_2O_2. a) Schematic depiction of immobilized sensing platform, where the nanosensor is incubated in a glass microwell dish for 20 min, washed, and rehydrated with 1X PBS before analyte addition and imaging. Addition of analyte induces an increase in fluorescence intensity of the sensor. b) Analysis of fluorescence microscopy images of immobilized nanosensor over 5 min shows ≈15% increase in fluorescence intensity corresponding to H_2O_2 addition at 120 s. c) Fluorescence microscopy image of immobilized nanosensor at 9 s post-hydration with PBS. d) Fluorescence microscopy image of immobilized nanosensor at 4 s post-addition of H_2O_2 shows increased fluorescence intensity compared to (c). e) Analysis of fluorescence microscopy images of immobilized nanosensor over 10 min shows repeatable fluorescence intensity increase upon subsequent additions of H_2O_2. f) Fluorescence microscopy image of immobilized nanosensor at 9 s post-hydration with PBS. g) Fluorescence microscopy image of immobilized nanosensor at 4 s post the third addition of H_2O_2 shows increased fluorescence intensity compared to (f). Gray shaded areas represent the standard deviation from the mean value in black ($n = 20$). Average fluorescence change values in (b) and (e) are calculated using ROIs from the entire image field of view. Images in (c), (d), (f), and (g) are representative images highlighting the center of the field of view and capture fluorescence intensity emitted by the SWCNTs from 900–1700 nm through a 900 nm long-pass filter.

2.4. Immobilized Nanosensor Response to Analyte

After characterizing the solution-phase nanosensor response, we investigated the nanosensor response when surface-immobilized on a glass microwell dish (**Figure** 4a). HRP-$(GT)_{15}$-SWCNTs were immobilized on a glass microwell dish and imaged after rehydration with PBS over the course of 5 min. Isolating the image analysis to fluorescent HRP-$(GT)_{15}$-SWCNT regions of interest with high fluorescence and averaging their values over time, we demonstrate the nanosensor's ability to sense hydrogen peroxide when immobilized through an imaging format (Figure 4b). The addition of water at 60 s shows no measurable fluorescence change, while the addition of 588 µM H_2O_2 at 120 s shows a signal increase of ≈15%, with representative images at Frame 9 (Figure 4c) and 124 (Figure 4d). This response can thus still be attributed to the analyte's presence upon addition rather than volume increases.

Further, the repeatability of this response can be seen by the similar sharp increases in fluorescence upon subsequent additions of H_2O_2 every 120 s (Figure 4e). The fluorescence intensity increases for each addition by a similar magnitude, suggesting that the consumption of analyte by HRP is modulating SWCNT fluorescence intensity rather than an interaction between the analyte or reaction byproducts and the SWCNT itself. In the context of the mechanism proposed in Section 2.3, the low concentration of H_2O_2 added would rapidly induce the heme center of HRP to its Compound II or Compound III form before its decay to native enzyme, causing the observed immediate fluorescence increase followed by a gradual decay. The signal fails to fully return to baseline between analyte additions likely due to imaging drift, where the addition of buffer and analyte to the microwell dish adds weight that shifts the imaging plane downwards from its original location, causing a drift in the measured baseline intensity. The visual presence of SWCNTs in the image after H_2O_2
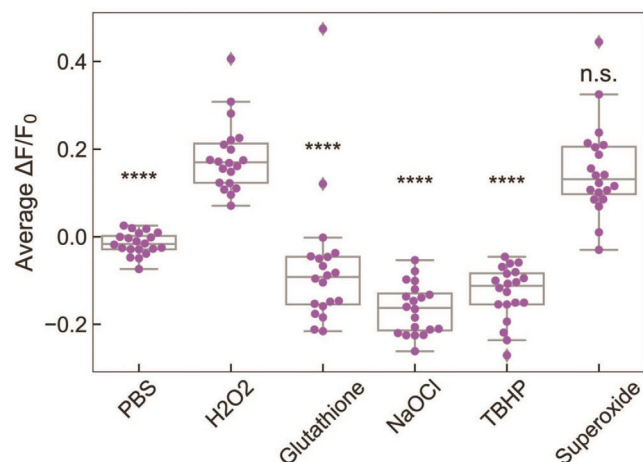
**ADVANCED
SCIENCE NEWS**

www.advancedsciencenews.com

**ADVANCED
FUNCTIONAL
MATERIALS**

www.afm-journal.de

Figure 5. Nanosensor selectivity against relevant analytes. Normalized change in fluorescence values of nanosensor immobilized on glass upon addition of analytes shows minimal response for analytes other than the target. Fluorescence change for each ROI ($n = 20$) 10 s after analyte addition is plotted as purple circles for each condition. ****$P = 3.35 \times 10^{-9}$ (PBS), 1.64×10^{-13} (Glutathione), 2.26×10^{-14} (NaOCl), and 2.26×10^{-14} (TBHP), and $P = 0.89$ (Superoxide) in independent two-sample t tests for each analyte $\Delta F/F_0$ in comparison to H_2O_2.

addition (Figure 4g) confirms that the immobilized nanosensors are not degrading over the course of the experiment, as does the persistence of stable spectroscopy nanosensor fluorescence (Figure 3d). The difference in magnitude of fluorescence modulation between the solution phase HRP-(GT)$_{15}$-SWCNT nanosensor response to hydrogen peroxide and this immobilized form factor can be attributed to the difference in analysis between the two. In solution, the fluorescence is measured for each wavelength in the nIR region, whereas the immobilized form factor captures fluorescence images of the sample, aggregating the total emission over the nIR region into an image. The solution-phase response is stronger at certain nIR wavelengths (Figure 3c), corresponding to different chirality SWCNTs. This sensitivity is lost in the images as they only capture overall emission, limiting the magnitude of the response to the same concentration of H_2O_2.

2.5. Nanosensor Analyte Selectivity

Following successful demonstration of the surface-immobilized nanosensor, we next characterized the HRP-(GT)$_{15}$-SWCNT nanosensor's selectivity for H_2O_2 against a panel of relevant analytes (**Figure 5**). These analytes were chosen to both ensure that the catalysis of H_2O_2 was the sole signal source rather than similar structural analogues (TBHP) or downstream reaction intermediates (superoxide), and to evaluate the potential interference of biomolecules that would be present during in vitro sensing applications (GSH and sodium hypochlorite). Compared to buffer and H_2O_2 control, the addition of 50 μm of GSH, NaOCl, and TBHP produced either no response or a turn-off response. The addition of 50 μm of superoxide did produce a turn-on response similar to H_2O_2, though this result is expected as superoxide bound to the heme core of HRP is an intermediate of the enzyme's catalytic cycle (Compound III), further supporting

our proposed mechanism for the nanosensor.[73,74] Altogether, our nanosensor appears to be selective for ROS over other potential interfering species, further confirming the necessity of HRP-analyte interaction for the observed fluorescence turn-on response. Further relevant analytes can be quickly assayed using the immobilized form factor depending on the intended application.

3. Conclusion

The generation of SWCNT-based nanosensors has been important to enable the visualization of biological analytes through the unique near-infrared fluorescence of SWCNTs. One outstanding challenge in the development of SWCNT-based nanosensors lies in identifying suitable molecular recognition elements to provide analyte-selective modulation of SWCNT fluorescence. Direct attachment of protein-based molecular recognition agents would enable a design-based approach to nanosensor development so long as protein function and SWCNT intrinsic fluorescence can both be preserved. In this work, we show that triazine-based SWCNT functionalization can be used to attach HRP enzymes to SWCNTs and demonstrate H_2O_2 sensing as a proof-of-principle demonstration of nanosensor functionality. To generate these sensors, we leveraged triazine-based SWCNT functionalization to attach free thiol groups to pristine SWCNTs while maintaining the SWCNT optical properties. We determined that the resulting HRP-(GT)$_{15}$-SWCNT nanosensor showed a concentration-dependent turn-on fluorescence response to H_2O_2 in solution, partly due to the quenched SWCNT fluorescence baseline intensity after HRP conjugation. Fitting this response to a cooperative binding model produced estimated kinetic parameters including a solution-phase LOD of 31 μm. Though this value is above typical cellular ROS levels (100 nm–10 μm),[75] the nanosensor showed the ability to sense H_2O_2 when surface-immobilized on glass, presenting an alternate viable sensing form factor for effective H_2O_2 sensing in other systems with higher H_2O_2 levels such as contaminated water samples and food production.[31] In this imaging form factor, the nanosensor showed robust analyte selectivity against similar analytes. Taken together, this study demonstrates the potential of covalent protein-SWCNT nanosensors for sensitive, specific, and stable analyte sensing and imaging.

The nanosensor synthesis platform developed here can also be extended to conjugate other proteins and enzymes of interest and generate robust nanosensors for biologically relevant analytes. The use of Sulfo-SMCC as the cross-linking agent allows any protein with exposed primary amines to be a candidate for conjugation to SH-SWCNTs. Additionally, the use of Triazine-SWCNT chemistry provides a wide library of available SWCNT surface functional groups like carboxylic acids (-COOH), primary amines (-NH$_2$), and biotin. These functionalized SWCNTs could thus be used with other cross-linker systems to conjugate proteins that are not amenable to maleimide functionalization via Sulfo-SMCC. While our approach for using covalent conjugation of enzymes to SWCNT could be generalizable for other enzymes and possibly also antibodies, we note that ensuring proper quality control of the nanosensor product is imperative for downstream use. For instance, commercially-procured enzymes and antibodies have been reported to have variable levels of activity, which could compromise the reproducibility

**ADVANCED
SCIENCE NEWS**

www.advancedsciencenews.com

**ADVANCED
FUNCTIONAL
MATERIALS**

www.afm-journal.de

of the nanosensor product.[76–80] Furthermore, proteins are also known to have variable levels of intrinsic affinity for the SWCNT surface.[81,82] Therefore, it is important to assess both the level of enzyme non-specific binding to the SWCNT surface and the level of enzymatic or binding activity of the final nanosensor product[17] to ensure the response originates from covalently-attached proteins.[17] Orthogonally, SWCNTs are also confirmed to be valuable as biomolecule delivery agents,[83–86] and our conjugation work herein could enable protein conjugation to SWCNTs for protein delivery applications. Ultimately, these nanosensors could help advance the use of SWCNTs as nanomaterials for theranostics, delivery, and cellular fluorescence imaging purposes.

4. Experimental Section

Materials: All chemicals unless otherwise stated were purchased from Sigma-Aldrich. Raw high pressure carbon monoxide (HiPco) synthesized SWCNTs were purchased from NanoIntegris (SKU# 1601). C_{16}-PEG(2000)-Ceramide (N-palmitoyl-sphingosine-1-{succinyl[methoxy(polyethyleneglycol)2000]}) was purchased from Avanti Polar Lipids (SKU# 880180P). $(GT)_{15}$ ssDNA was purchased from Integrated DNA Technologies. Sulfo-SMCC (sulfosuccinimidyl 4-(N-maleimidomethyl)cyclohexane-1-carboxylate) was purchased from ThermoFisher Scientific (Catalog# A39268). Luminol (Pierce ECL Western Blotting Substrate) was purchased from ThermoFisher Scientific (Catalog# 32 209). Glass-bottom microwell dishes (35 mm petri dish with 10 mm microwell) were purchased from MatTek (Catalog# NC9341562). Hydrogen Peroxide (3% w/w) was purchased from Labchem (Catalog# LC154501). Sodium hypochlorite was purchased from Avantor Performance Materials (Catalog# 9416-01). Tert-butyl hydroperoxide (TBHP) was purchased from EMD Millipore (Catalog# 8.14006.0250). Xanthine was purchased from Sigma-Aldrich (Catalog# X7375-25G). Xanthine Oxidase (from buttermilk) was purchased from Millipore Sigma (Catalog# 682151-10U). 2-(2-methoxy-4-nitrophenyl)—3-(4-nitrophenyl)—5-(2,4-disulfophenyl)—2H-tetrazolium (WST-8) was purchased from MedChemExpress (Catalog# HY-D0831-25MG).

Synthesis of SH-Functionalized SWCNTs: Synthesis of SH-functionalized SWCNTs was adapted from previous literature.[27,29] Briefly, pristine HiPco SWCNTs (1 g) were dispersed in N-methyl-2-pyrrolidone (NMP) (150 mL) in a round bottom flask with a stir bar. The mixture was bath sonicated (Branson Ultrasonic 1800) for 1 h at 25 °C followed by gentle stirring for 1 h at 25 °C. The mixture was then cooled to 0 °C on ice. 2,4,6-1,3,5-trichloro-triazine (10 g, 54 mmol) was dissolved in NMP (50 mL) and slowly added to the SWCNT dispersion. The resulting mixture was stirred for 20 min at 0 °C. Sodium azide (1.76 g, 27 mmol) was gradually added to the mixture and stirred for 2 h at 0 °C. The mixture was then stirred at 25 °C for 1 h followed by stirring at 70 °C for 12 h to yield Trz-H-SWCNTs. This product was purified by repeated centrifugation and washing steps with 10 mL each of acetone, water, toluene, then chloroform. The purified product was then lyophilized for storage and characterization.

Trz-H-SWCNTs (10 mg) were dispersed in dimethylformamide (DMF) (5 mL) and bath sonicated for 15 min at 25 °C. Cysteine (1 mg) and a 1.5 M excess of triethylamine were added to the mixture and stirred for 48 h at 65 °C. The product (SH-SWCNTs) was purified by centrifugation, supernatant removal, and re-dispersion in washes of DMF (4 mL, 2X) then water (4 mL, 2X). The product was then dialyzed against water using a Slide-A-Lyzer G2 10 kDa MWCO dialysis cassette (Thermo Scientific) for 1 week with daily water changes (2 L). The purified product was pelleted by centrifugation and lyophilized for storage, characterization, and covalent HRP functionalization.

Noncovalent Adsorption of ssDNA to SH-SWCNTs by Probe-Tip Sonication: SH-SWCNTs (1 mg) and $(GT)_{15}$ single-stranded DNA (1 mg) were dispersed in 1X phosphate buffered saline (PBS) (500 µL, pH 7.4) and bath sonicated for 10 min at 25 °C. The solution was then probe-tip sonicated with an ultrasonic processor (Cole Parmer) and a 3 mm stepped

microtip probe with pulses of 3–7 W for 1 s followed by 2 s of rest for a total sonication time of 15 min. The solution was equilibrated for 1 h at 25 °C then subsequently centrifuged at 16100 relative centrifugal force (RCF) for 30 min to remove unsuspended SWCNT aggregates. Suspended SWCNTs formed a homogeneous dark gray solution and were measured for concentration by UV–Vis–IR absorbance (Shimadzu UV-3600 Plus) with samples in a 100 µL volume, black-sided quartz cuvette (Thorlabs, Inc.). SWCNT concentration was calculated from absorbance at 632 nm using the Beer-Lambert law with extinction coefficient $\epsilon_{632} = 0.036$ L mg^{-1} cm^{-1}.[87]

Corona Exchange Dynamics Assay for HRP-SWCNT Adsorption: Corona exchange dynamics studies were conducted as described previously.[17] Briefly, HRP, fibrinogen, and human serum albumin were labeled with a fluorophore (FAM) via N-hydroxysuccinimide ester conjugation (Lumiprobe). Protein (10 mg) in 1X PBS (900 µL) and an eight-fold molar excess of FAM-NHS in dimethyl sulfoxide (DMSO) (100 µL) were gently mixed via end-over-end rotation in a foil-covered tube for 4 h. FAM-protein conjugates were then purified with Zeba 2 mL spin desalting columns with 40 kDa MWCO (Thermo Scientific) to remove excess unreacted FAM-NHS according to manufacturer's instructions. The purified FAM-proteins were measured for concentration and degree of labeling via UV–Vis–IR absorbance at 280 nm for protein and 495 nm for FAM. The degree of labeling was calculated as the molar ratio of FAM to protein in the samples. 200 mg L^{-1} FAM fluorophore-labeled protein (25 µL) was added to 10 mg L^{-1} SH-SWCNTs dispersed with $(GT)_{15}$ ssDNA, C_{16}-PEG2k-Ceramide, and SC (25 µL) in triplicate. The solutions were combined via microchannel pipette in a 96-well PCR plate (Bio-Rad) and mixed by pipetting. The plate was sealed with an optically transparent adhesive seal and gently spun down in a benchtop centrifuge. Fluorescence time series measurements were obtained with a Bio-Rad CFX96 Real Time qPCR System by scanning the FAM channel every 30 s at 25 °C.

Covalent Conjugation of HRP to SH-SWCNT via Sulfo-SMCC Cross-Linker: $(GT)_{15}$-SH-SWCNTs were diluted to 20 mg L^{-1} in PBS and 5% v/v TCEP to reduce disulfide bonds between SWCNTs. HRP was similarly diluted to 2 mg mL^{-1} in PBS and Sulfo-SMCC dissolved in Milli-Q H_2O was added at 10:1 molar ratio Sulfo-SMCC:HRP. Both mixtures were incubated separately for 1 h at 25 °C. Each solution was then de-salted to remove excess TCEP and Sulfo-SMCC, respectively, with 7 K MWCO Zeba Spin Desalting Columns (2 mL) according to manufacturer's instructions. Purified $(GT)_{15}$-SH-SWCNTs and maleimide-functionalized HRP were then mixed at a final concentration of 10 and 1 mg mL^{-1}, respectively, and incubated 1 h at 25 °C. The finished reaction mixture was purified to remove unconjugated maleimide-HRP with 100 K MWCO Amicon Ultra Centrifugal Filters (0.5 mL). The membrane was rinsed with PBS and centrifuged at 5000 rcf for 5 min. The raw reaction mixture was then added and spun at the same conditions. PBS (450 µL) was added to the membrane to wash away excess protein and spun at the same conditions and repeated once. Finally, the membrane was cleaned with PBS (200 µL) to remove adsorbed SWCNTs and the membrane was inverted and spun at 1000 rcf for 2 min to collect the purified sample. The recovered HRP-$(GT)_{15}$-SWCNTs were then diluted to their original reaction volume and characterized by UV–Vis–IR absorbance and nIR fluorescence measurements.

Atomic Force Microscopy of SWCNT Nanosensors: SWCNT nanosensors were analyzed for the presence of HRP with atomic force microscopy (AFM). A small square (1 cm x 1 cm) of mica substrate was adhered to a glass slide and the top surface was freshly cleaved with tape immediately prior to sample preparation. HRP-$(GT)_{15}$-SWCNT (100 µL) at 5 mg L^{-1} in 1X PBS was statically dispensed onto the mica surface and spin-coated at 2000 rpm for 1 min. Static dispense and spin coating was then repeated with an additional 100 µL of 5 mg L^{-1} HRP-$(GT)_{15}$-SWCNT to increase the coverage of functionalized SWCNT on the mica surface. Once doubly coated, deionized water (100 µL) was slowly dynamically dispensed onto the coated surface while spinning to rinse off excess salts. The sample was then stored at room temperature overnight and imaged using a TAP150AL-G (Ted Pella) Aluminum Reflex coated tip coupled to an MFP-3D-BIO AFM (Asylum Research) in soft tapping mode.

Luminol Assay for HRP Activity: HRP activity was assessed using the Pierce ECL Western Blotting Substrate kit. Briefly, the samples were all diluted to the same HRP concentration as the lowest concentration to

be measured for activity, typically the nanosensor. Each sample was confirmed to be at the correct [HRP] via Qubit assay according to manufacturer's instructions. The peroxide and luminol stocks from the kit were mixed at 1:1 by volume and added to each sample to dilute the [HRP] to the working concentration of 0.5 mg L^{-1} according to the manufacturer's instructions. Each sample (50 μL) was added to a 96-well plate in triplicate and the luminescence of each well was measured over 60 min on a luminescence plate reader (Tecan M1000).

Near-Infrared Spectroscopy of SWCNT Nanosensors: Fluorescence spectra were obtained with an in-house nIR microscope setup. Briefly, an inverted Zeiss microscope (Axio Observer.D1, 10X objective) coupled to a Princeton Instruments spectrometer (SCT 320) and liquid nitrogen-cooled Princeton Instruments InGaAs detector (PyLoN-IR) was used. SWCNT samples were excited with a 721 nm laser (OptoEngine LLC) and emission was collected in the 850 – 1350 nm wavelength range. The samples were measured in a 384 well-plate (Greiner Bio-One microplate) with a total volume of 30 μL per well. For solution-phase sensor response screens, nanosensor at 2.5 mg L^{-1} [SWCNT] in 1X PBS (27 μL) was added per well and 10X H$_2$O$_2$ (3 μL) was injected per well with a microchannel pipette in triplicate. After analyte addition, each well was briefly mixed by pipetting, sealed with an adhesive seal (Bio-Rad), and spun down for 10 s with a benchtop well plate centrifuge to remove bubbles. Fluorescence spectra were measured at time points of 0 min after analyte addition, 5, 10, 15, 20 min, and every 10 min after until 1 h post-addition.

Near-Infrared Microscopy of SWCNT Nanosensors: Fluorescence images were captured with the same epifluorescence microscope setup as described previously with a 100X oil immersion objective and a Ninox VIS-SWIR 640 camera (Raptor). Nanosensors were immobilized on glass-bottom microwell dishes (35 mm petri dish with 10 mm microwell, MatTek) as follows: each dish was washed twice with PBS (150 μL), incubated with nanosensor at 2.5 mg L^{-1} (100 μL) for 20 min, and washed twice again with PBS (150 μL). For each image, PBS (160 μL) was added to the dish and the z-plane was refocused to maximize SWCNT fluorescence intensity. Images were then recorded over 5 min with an exposure time of 950 and 1000 ms repeat cycle. Water (20 μL) was added at Frame 60 and analyte (20 μL) was added at Frame 120. Images were processed with ImageJ as follows: a median filter (0.5-pixel radius) and rolling ball background subtraction (300-pixel radius) were applied, the image was cropped to eliminate gaussian blur and highlight the center of the image with the brightest nanosensors (width = 375, height = 375, x-coordinate = 110, y-coordinate = 36), the image was then analyzed using the ROI analyzer tool (Multi Measure) highlighting the clearest 20 ROIs of nanosensor bundles.

Superoxide Generation: Superoxide was generated enzymatically with the Xanthine/Xanthine Oxidase system according to previously established protocols.[74] Briefly, Xanthine was dissolved at 10 mM in 0.1 M NaOH and the pH was adjusted to 7 with 0.1 M HCl and a pH probe. Xanthine Oxidase was diluted to 0.1 U mL^{-1} in 1X PBS. Xanthine and Xanthine Oxidase (50 μL each) were added to 1X PBS (140 μL) in an Eppendorf tube and incubated 2 h at 25 °C. Separately, the generation of superoxide was validated by incubating 20 mg mL^{-1} WST-8 with the reaction mixture. The absorbance at 460 nm of the resulting solution was measured to determine the presence of the WST-8 formazan product, which was proportional to the generation of superoxide. Using the Beer-Lambert law with extinction coefficient $\epsilon_{460} = 30700$ M^{-1} cm^{-1} for the formazan product and knowing 2 superoxide radicals were required to generate 1 formazan, the superoxide concentration in this system was calculated (Figure S15, Supporting Information).[88]

SDS-PAGE of Nanosensors and Filtration Flowthroughs: SDS-PAGE was performed according to previously established protocols. Briefly, sample buffer was prepared by combining glycerol (2.5 mL), water (3.75 mL), 0.5 M Tris-HCl buffer pH 6.8 (1.25 mL), and 10% w/v SDS (2 mL). Gel running buffer was prepared with 10X Tris/Glycine/SDS Buffer (50 mL, Bio-Rad) and deionized water (450 mL). Sample (5 μL) was added to sample buffer (7.5 μL) and 6X loading dye (2.5 μL, New England Biosciences) and boiled at 95 °C for 5 min. Samples were then loaded onto a 4–20% Mini-PROTEAN TGX Precast Protein Gel (Bio-Rad) in a Mini-PROTEAN Tetra Vertical Electrophoresis Cell (Bio-Rad) with running buffer according

to manufacturer's instructions. Gel electrophoresis was run with a Mini-PROTEAN PowerPac Basic Power Supply (Bio-Rad) at 200 V for 30 min. The finished gel was then stained with Coomassie Brilliant Blue (Thermo Scientific) for 1 h, shaking gently. The gel was then de-stained overnight with 50% water, 40% methanol, 10% acetic acid (v/v/v) solution. The final gel was rehydrated in water and imaged according to manufacturer's instructions on a Typhoon FLA 9500 laser scanner (Cytiva) in digitization mode with a 532 nm excitation laser and a long-pass green filter. Gel images were processed with imageJ to adjust color contrast and image field of view.

Supporting Information

Supporting Information is available from the Wiley Online Library or from the author.

Acknowledgements

Conflict of Interest

The authors declare no conflict of interest.

Data Availability Statement

The data that support the findings of this study are available from the corresponding author upon reasonable request.

Keywords

[1] Z. Liu, S. Tabakman, K. Welsher, H. Dai, *Nano Res.* **2009**, *2*, 85.

[2] M. J. O'Connell, S. M. Bachilo, C. B. Huffman, V. C. Moore, M. S. Strano, E. H. Haroz, K. L. Rialon, P. J. Boul, W. H. Noon, C. Kittrell, J. Ma, R. H. Hauge, R. B. Weisman, R. E. Smalley, *Science* **2002**, *297*, 593.

[3] J. Frangioni, *Curr. Opin. Chem. Biol.* **2003**, *7*, 626.

[4] J. Zhang, M. P. Landry, P. W. Barone, J.-H. Kim, S. Lin, Z. W. Ulissi, D. Lin, B. Mu, A. A. Boghossian, A. J. Hilmer, A. Rwei, A. C. Hinckley, S. Kruss, M. A. Shandell, N. Nair, S. Blake, F. Şen, S. Şen, R. G. Croy, D. Li, K. Yum, J.-H. Ahn, H. Jin, D. A. Heller, J. M. Essigmann, D. Blankschtein, M. S. Strano, *Nat. Nanotechnol.* **2013**, *8*, 959.

[5] J. Ackermann, J. T. Metternich, S. Herbertz, S. Kruss, *Angew. Chem., Int. Ed.* **2022**, *61*, 202112372.

[6] S. Jeong, D. Yang, A. G. Beyene, J. T. Del Bonis-O'Donnell, A. Gest, N. Navarro, X. Sun, M. P. Landry, *Sci. Adv.* **2019**, *5*, aay3771.

[7] G. Bisker, J. Dong, H. D. Park, N. M. Iverson, J. Ahn, J. T. Nelson, M. P. Landry, S. Kruss, M. S. Strano, *Nat. Commun.* **2016**, *7*, 10241.

[8] G. Bisker, N. A. Bakh, M. A. Lee, J. Ahn, M. Park, E. B. O'Connell, N. M. Iverson, M. S. Strano, *ACS Sens.* **2018**, *3*, 367.

[9] L. Chio, J. T. Del Bonis-O'Donnell, M. A. Kline, J. H. Kim, I. R. McFarlane, R. N. Zuckermann, M. P. Landry, *Nano Lett.* **2019**, *19*, 7563.

[10] A. Antonucci, J. Kupis-Rozmysłowicz, A. A. Boghossian, *ACS Appl. Mater. Interfaces* **2017**, *9*, 11321.

[11] P. W. Barone, S. Baik, D. A. Heller, M. S. Strano, *Nat. Mater.* **2005**, *4*, 86.

[12] S. Kruss, M. P. Landry, E. Vander Ende, B. M. A. Lima, N. F. Reuel, J. Zhang, J. Nelson, B. Mu, A. Hilmer, M. Strano, *J. Am. Chem. Soc.* **2014**, *136*, 713.

[13] F. Ledesma, B. Ozcan, X. Sun, S. M. Medina, M. P. Landry, *Adv. Funct. Mater.* **2022**, *32*, 2107174.

[14] S. S. Karajanagi, A. A. Vertegel, R. S. Kane, J. S. Dordick, *Langmuir* **2004**, *20*, 11594.

[15] K. Matsuura, T. Saito, T. Okazaki, S. Ohshima, M. Yumura, S. Iijima, *Chem. Phys. Lett.* **2006**, *429*, 497.

[16] R. A. Graff, J. P. Swanson, P. W. Barone, S. Baik, D. A. Heller, M. S. Strano, *Adv. Mater.* **2005**, *17*, 980.

[17] R. L. Pinals, D. Yang, A. Lui, W. Cao, M. P. Landry, *J. Am. Chem. Soc.* **2020**, *142*, 1254.

[18] N. R. Palwai, D. E. Martyn, L. F. F. Neves, Y. Tan, D. E. Resasco, R. G. Harrison, *Nanotechnology* **2007**, *18*, 235601.

[19] M. M. Noor, J. Goswami, V. A. Davis, *ACS Omega* **2020**, *5*, 2254.

[20] S. Kruss, A. J. Hilmer, J. Zhang, N. F. Reuel, B. Mu, M. S. Strano, *Adv. Drug Delivery Rev.* **2013**, *65*, 1933.

[21] A. Hirsch, *Angew. Chem., Int. Ed.* **2002**, *41*, 1853.

[22] L. Cognet, D. A. Tsyboulski, J.-D. R. Rocha, C. D. Doyle, J. M. Tour, R. B. Weisman, *Science* **2007**, *316*, 1465.

[23] S. Ghosh, S. M. Bachilo, R. A. Simonette, K. M. Beckingham, R. B. Weisman, *Science* **2010**, *330*, 1656.

[24] Y. Piao, B. Meany, L. R. Powell, N. Valley, H. Kwon, G. C. Schatz, Y. Wang, *Nat. Chem.* **2013**, *5*, 840.

[25] F. A. Mann, N. Herrmann, F. Opazo, S. Kruss, *Angew. Chem., Int. Ed.* **2020**, *59*, 17732.

[26] F. A. Mann, P. Galonska, N. Herrmann, S. Kruss, *Nat. Protoc.* **2022**, *17*, 727.

[27] A. Setaro, M. Adeli, M. Glaeske, D. Przyrembel, T. Bisswanger, G. Gordeev, F. Maschietto, A. Faghani, B. Paulus, M. Weinelt, R. Arenal, R. Haag, S. Reich, *Nat. Commun.* **2017**, *8*, 14281.

[28] A. G. Godin, A. Setaro, M. Gandil, R. Haag, M. Adeli, S. Reich, L. Cognet, *Sci. Adv.* **2019**, *5*, aax1166.

[29] L. Chio, R. L. Pinals, A. Murali, N. S. Goh, M. P. Landry, *Adv. Funct. Mater.* **2020**, *30*, 1910556.

[30] J. F. Woolley, J. Stanicka, T. G. Cotter, *Trends Biochem. Sci.* **2013**, *38*, 556.

[31] J. E. Giaretta, H. Duan, F. Oveissi, S. Farajikhah, F. Dehghani, S. Naficy, *ACS Appl. Mater. Interfaces* **2022**, *14*, 20491.

[32] R. L. Pinals, F. Ledesma, D. Yang, N. Navarro, S. Jeong, J. E. Pak, L. Kuo, Y.-C. Chuang, Y.-W. Cheng, H.-Y. Sun, M. P. Landry, *Nano Lett.* **2021**, *21*, 2272.

[33] M. Gajhede, D. J. Schuller, A. Henriksen, A. T. Smith, T. L. Poulos, *Nat. Struct. Mol. Biol.* **1997**, *4*, 1032.

[34] A. M. O'Brien, C. Ó'Fágáin, P. F. Nielsen, K. G. Welinder, *Biotechnol. Bioeng.* **2001**, *76*, 277.

[35] S. Nishitani, T. Tran, A. Puglise, S. Yang, M. P. Landry, *Angew. Chem.* **2023**, *63*, 202311476.

[36] T. T. S. Lew, V. B. Koman, K. S. Silmore, J. S. Seo, P. Gordiichuk, S.-Y. Kwak, M. Park, M. C.-Y. Ang, D. T. Khong, M. A. Lee, M. B. Chan-Park, N.-H. Chua, M. S. Strano, *Nat. Plants* **2020**, *6*, 404.

[37] A. Jorio, R. Saito, T. Hertel, R. B. Weisman, G. Dresselhaus, M. S. Dresselhaus, *MRS Bull.* **2004**, *29*, 276.

[38] M. S. Dresselhaus, G. Dresselhaus, R. Saito, A. Jorio, *Annu. Rev. Phys. Chem.* **2007**, *58*, 719.

[39] D. A. Heller, G. W. Pratt, J. Zhang, N. Nair, A. J. Hansborough, A. A. Boghossian, N. F. Reuel, P. W. Barone, M. S. Strano, *Proc. Natl. Acad. Sci. USA* **2011**, *108*, 8544.

[40] J. J. Brege, C. Gallaway, A. R. Barron, *J. Phys. Chem. C* **2007**, *111*, 17812.

[41] C. P. Horozko, P. J. Schnatz, J. Budhathoki-Uprety, R. V. Rao-Pothuraju, R. L. Koder, D. A. Heller, *ACS Appl. Mater. Interfaces* **2021**, *13*, 51343.

[42] K. G. Welinder, *Eur. J. Biochem.* **1979**, *96*, 483.

[43] A. Kessler, J. Hedberg, S. McCarrick, H. L. Karlsson, E. Blomberg, I. Odnevall, *Chem. Res. Toxicol.* **2021**, *34*, 1481.

[44] H. Zhu, Z. Jia, M. Trush, Y. R. Li, *React. Oxyg. Species* **2016**, *1*, 216.

[45] R. Sariri, R. H. Sajedi, V. Jafarian, *J. Mol. Liq.* **2006**, *123*, 20.

[46] E. Ochoe de Aspuru, A. M. Lourdes Zatón, *Spectrochim. Acta, Part A* **1999**, *55*, 2343.

[47] D. E. Heck, M. Shakarjian, H. D. Kim, J. D. Laskin, A. M. Vetrano, *Ann. N. Y. Acad. Sci.* **2010**, *1203*, 120.

[48] J. N. Rodríguez-López, D. J. Lowe, J. Hernández-Ruiz, A. N. P. Hiner, F. García-Cánovas, R. N. F. Thorneley, *J. Am. Chem. Soc.* **2001**, *123*, 11838.

[49] P. Bollella, L. Medici, M. Tessema, A. A. Poloznikov, D. M. Hushpulian, V. I. Tishkov, R. Andreu, D. Leech, N. Megersa, M. Marcaccio, L. Gorton, R. Antiochia, *Solid State Ionics* **2018**, *314*, 178.

[50] C. Ruan, F. Yang, C. Lei, J. Deng, *Anal. Chem.* **1998**, *70*, 1721.

[51] J. Kruusma, V. Sammelselg, C. E. Banks, *Electrochem. Commun.* **2008**, *10*, 1872.

[52] A. Navas Diáz, M. C. Ramos Peinado, M. C. Torijas Minguez, *Anal. Chim. Acta* **1998**, *363*, 221.

[53] L. Jiao, W. Xu, H. Yan, Y. Wu, C. Liu, D. Du, Y. Lin, C. Zhu, *Anal. Chem.* **2019**, *91*, 11994.

[54] P. Qian, Y. Qin, Y. Lyu, Y. Li, L. Wang, S. Wang, Y. Liu, *Anal. Bioanal. Chem.* **2019**, *411*, 1517.

[55] C. K. Tagad, S. R. Dugasani, R. Aiyer, S. Park, A. Kulkarni, S. Sabharwal, *Sens. Actuators, B* **2013**, *183*, 144.

[56] P. Bauduin, F. Nohmie, D. Touraud, R. Neueder, W. Kunz, B. W. Ninham, *J. Mol. Liq.* **2006**, *123*, 14.

[57] A. Bhandari, W. Kim, K. Hohn, *J. Environ. Eng.* **2010**, *136*, 1147.

[58] W. Sun, X. Ji, L. J. Kricka, H. B. Dunford, *Can. J. Chem.* **1994**, *72*, 2159.

[59] D. Morales-Urrea, A. López-Córdoba, E. M. Contreras, *Sci. Rep.* **2023**, *13*, 13363.

[60] K. Nazari, A. Mahmoudi, M. Shahrooz, R. Khodafarin, A. A. Moosavi-Movahedi, *J. Enzyme Inhib. Med. Chem.* **2005**, *20*, 285.

[61] J. Vlasits, C. Jakopitsch, M. Bernroitner, M. Zamocky, P. G. Furtmüller, C. Obinger, *Arch. Biochem. Biophys.* **2010**, *500*, 74.

[62] J. Hernández-Ruiz, M. B. Arnao, A. N. P. Hiner, F. García-Cánovas, M. Acosta, *Biochem. J.* **2001**, *354*, 107.

[63] L. Mao, S. Luo, Q. Huang, J. Lu, *Sci. Rep.* **2013**, *3*, 3126.

[64] S. Han, Y. Cui, D. L. Helbing, *Biotechnol. J.* **2020**, *15*, 1900397.

[65] M. A. Orlova, E. A. Mareeva, V. V. Doseeva, Y. L. Kapeliukh, L. G. Gazaryan, O. A. Kost, *Russ. Chem. Bull.* **1995**, *44*, 172.

[66] K. J. Baynton, J. K. Bewtra, N. Biswas, K. E. Taylor, *Biochim. Biophys. Acta* **1994**, *1206*, 272.

[67] R. Nakajima, I. Yamazaki, *J. Biol. Chem.* **1987**, *262*, 2576.

[68] S. O. Malomo, R. I. Adeoye, L. Babatunde, I. A. Saheed, M. O. Iniaghe, F. J. Olorunniji, *Biokemistri* **2011**, *23*, 124.

[69] T. Kawano, S. Muto, M. Adachi, H. Hosoya, F. Lapeyrie, *Biosci., Biotechnol., Biochem.* **2002**, *66*, 651.

**ADVANCED
SCIENCE NEWS**

www.advancedsciencenews.com

**ADVANCED
FUNCTIONAL
MATERIALS**

www.afm-journal.de

[70] T. Kawano, S. Muto, M. Adachi, H. Hosoya, F. Lapeyrie, *Biosci., Biotechnol., Biochem.* **2002**, *66*, 646.

[71] S. Steenken, S. V. Jovanovic, *J. Am. Chem. Soc.* **1997**, *119*, 617.

[72] A. A. Moosavi-Movahedi, K. Nazari, A. A. Saboury, *Colloids Surf., B* **1997**, *9*, 123.

[73] M. Kimura, Y. Umemoto, T. Kawano, *Front. Plant Sci.* **2014**, *5*, 00285.

[74] D. Metodiewa, H. B. Dunford, *Arch. Biochem. Biophys.* **1989**, *272*, 245.

[75] M. Giorgio, M. Trinei, E. Migliaccio, P. G. Pelicci, *Nat. Rev. Mol. Cell Biol.* **2007**, *8*, 722.

[76] J. E. Scott, K. P. Williams, in *Assay Guidance Manual* (Eds: S. Markossian, A. Grossman, M. Arkin, D. Auld, C. Austin, J. Baell, K. Brimacombe, T. D. Y. Chung, N. P. Coussens, J. L. Dahlin, V. Devanarayan, T. L. Foley, M. Glicksman, K. Gorshkov, J. V. Haas, M. D. Hall, S. Hoare, J. Inglese, P. W. Iversen, M. Lal-Nag, Z. Li, J. R. Manro, J. McGee, O. McManus, M. Pearson, T. Riss, P. Saradjian, G. S. Sittampalam, M. Tarselli, O. J. Trask), et al., Eli Lilly & Company and the National Center for Advancing Translational Sciences, Bethesda, MD **2004**.

[77] S. B. Rosalki, *Ann. Clin. Biochem.* **1980**, *17*, 74.

[78] C. Brandariz-Fontes, M. Camacho-Sanchez, C. Vilà, J. L. Vega-Pla, C. Rico, J. A. Leonard, *Sci. Rep.* **2015**, *5*, 8056.

[79] P. Acharya, A. Quinlan, V. Neumeister, *F1000Res* **2017**, *6*, 851.

[80] Y. Luo, M. Pehrsson, L. Langholm, M. Karsdal, A.-C. Bay-Jensen, S. Sun, *Diagnostics* **2023**, *13*, 1835.

[81] R. L. Pinals, D. Yang, D. J. Rosenberg, T. Chaudhary, A. R. Crothers, A. T. Iavarone, M. Hammel, M. P. Landry, *Angew. Chem., Int. Ed.* **2020**, *59*, 23668.

[82] N. Ouassil, R. L. Pinals, J. T. Del Bonis-O'Donnell, J. W. Wang, M. P. Landry, *Sci. Adv.* **2022**, *8*, abm0898.

[83] H. Zare, S. Ahmadi, A. Ghasemi, M. Ghanbari, N. Rabiee, M. Bagherzadeh, M. Karimi, T. J. Webster, M. R. Hamblin, E. Mostafavi, *Int. J. Nanomed.* **2021**, *16*, 1681.

[84] G. S. Demirer, H. Zhang, J. L. Matos, N. S. Goh, F. J. Cunningham, Y. Sung, R. Chang, A. J. Aditham, L. Chio, M.-J. Cho, B. Staskawicz, M. P. Landry, *Nat. Nanotechnol.* **2019**, *14*, 456.

[85] G. S. Demirer, H. Zhang, N. S. Goh, R. L. Pinals, R. Chang, M. P. Landry, *Sci. Adv.* **2020**, *6*, aaz0495.

[86] J. Chen, S. Chen, X. Zhao, L. V. Kuznetsova, S. S. Wong, I. Ojima, *J. Am. Chem. Soc.* **2008**, *130*, 16778.

[87] J. T. D. Bonis-O'Donnell, R. H. Page, A. G. Beyene, E. G. Tindall, I. R. McFarlane, M. P. Landry, *Adv. Funct. Mater.* **2017**, *27*, 1702112.

[88] K. Chamchoy, D. Pakotiprapha, P. Pumirat, U. Leartsakulpanich, U. Boonyuen, *BMC Biochem.* **2019**, *20*, 4.